



# Quantifying fatigue-damage and failure-precursors using ultrasonic coda wave interferometry

Guijie Sang, Shimin Liu<sup>\*</sup>, Derek Elsworth

Department of Energy and Mineral Engineering, G<sup>3</sup> Center and Energy Institute, The Pennsylvania State University, University Park, PA, 16802, USA

## ARTICLE INFO

### Keywords:

Coda wave interferometry  
Fatigue damage  
Cyclic compression  
Failure precursor  
Hardening effect  
Ultrasonic velocity

## ABSTRACT

Accumulation of the subtle impacts of fatigue-induced rock damage may ultimately trigger rock failure. Probing, understanding and quantifying this behavior is crucial in evaluating the mechanical response under dynamic loading. We conduct cyclic uniaxial compression tests with real-time measurement of ultrasonic velocity to probe the evolution of fatigue-induced damage in shale subjected to cycles of increasing-amplitude and constant-amplitude. The stress-strain response shows hysteretic behavior and hardening effect under cyclic compression. Time of first arrival is used to estimate apparent changes in ultrasonic velocity at incremented maximum stresses. Coda wave interferometry (CWI) is applied to detect the more subtle changes in ultrasonic velocity at minimum stress (10 MPa) under fatigue-loading. Despite a continuous increase in ultrasonic velocity measured at incremented maximum stresses the subtle signal of increasing fatigue-induced damage is apparent in the sensitive CWI signal. This is reflected in the descending trend of ultrasonic velocity, especially the S-wave velocity, observed at the minimum stress (10 MPa) – and may ultimately result in failure. The evolution of ultrasonic velocity is controlled by the competing effects of irreversible healing/closure of micro-fractures, dominating at low-stresses/early-cycles, and counteracted by the creation of fatigue-induced micro-fractures, dominating at high-stresses/late-cycles. The development of fatigue-induced micro-fractures is optimally detected by the multiply-scattered coda waves but is absent in the first arrivals. Dynamic modulus and relative changes in effective velocity inferred from CWI are sensitive and discernable indicators of fatigue-induced damage prior to failure while characteristics of the stress-strain curve and the evolution of elastic moduli are inferior indicators.

## 1. Introduction

Rock masses and structures on and in rock are typically subjected to repetitive natural and human-induced loads (Fig. 1). Natural loads include diurnal and seasonal changes in temperature and saturation, flooding, tides and earthquakes, with human-induced loading resulting from excavation, blasting, drilling, hydraulic fracturing and minor repetitive loads from rail and road traffic. Even minor loads, if repeated over sufficient cycles may accumulate damage and ultimately drive failure (Fig. 1) and present a hazard. Therefore, understanding the mechanical behavior of rock and rock masses subjected to repetitive dynamic loads is of great importance in quantifying and potentially predicting the occurrence and timing of the resulting hazards.<sup>1–3</sup> Despite extensive efforts to understand the mechanical behavior of rocks under static loading, the factors influencing fatigue response under dynamic and cyclic loading remain unclear due to the complex impact of various controlling factors including maximum stress, oscillatory-amplitude,

confining stress, loading frequency, water content, anisotropy, heterogeneity and sample size.<sup>1,4–12</sup> These factors compound to elevate the challenge in evaluating the mechanical response under dynamic and fatigue loading.

A variety of variables have been applied to estimate damage in rocks under cyclic loading conditions,<sup>3</sup> including measurements of volumetric deformation,<sup>13</sup> elastic/secant modulus,<sup>7,14</sup> acoustic emission (AE) counts,<sup>15</sup> dissipated energy,<sup>6</sup> permeability<sup>16</sup> and wave velocity.<sup>17,18</sup> Among these various signals, volumetric deformation, elastic/secant modulus, and energy dissipation can be extracted directly from the stress-strain response and are the most straightforward and effective indicators of evolving fatigue and damage. All provide a method to evaluate damage evolution and thus provide a way to predict rock integrity and failure behavior. Principal limitations are that all these parameters provide point measurements of response and only reflect macro-scale mechanical response without delineating internal defects. Permeability can also provide an understanding of fatigue-induced

<sup>\*</sup> Corresponding author.

E-mail address: [szl3@psu.edu](mailto:szl3@psu.edu) (S. Liu).

damage<sup>16</sup> if measured. As a damage develops, permeability typically increases due to the initiation of fracturing.<sup>16</sup> However, in heterogeneous rocks, including shales, typical signals of changes in fluid pressure are often insensitive to changes in permeability due to short-circuiting. Compared to these conventional static measurements of mechanical and transport properties as proxies for damage, monitoring of ultrasonic velocity and acoustic emission are two methods that both probe volumetrically and may simultaneously monitor micro-structural responses under dynamic loading. Between the two techniques, measurements of ultrasonic velocity provides an active non-destructive method to detect fatigue-induced internal defects. Thus, understanding the factors controlling the response of ultrasonic velocity to fatigue-induced internal damage provides a viable method of both delineating and quantifying damage evolution under repetitive loading conditions at field scale. As illustrated in Fig. 1, ultrasonic monitoring enables the state of the rock mass to be determined nondestructively.

Monitoring of ultrasonic wave speed has been used to study the fatigue behavior of natural rocks under cyclic loading.<sup>7,17–19</sup> Compressional wave propagation and AE activity in granites subjected to uniaxial cyclic compression<sup>17</sup> has shown that at maximum stress levels smaller than the dilatant strength of the rock, ultrasonic techniques are superior to AE methods in monitoring the progressive development of stress-induced cracks. A three-stage monotonic decay in the ultrasonic wave velocity is apparent in some granites relative to the number of loading cycles.<sup>7</sup> However, ultrasonic wave velocity is monitored at the maximum stress level of 0.8–0.95 of the static strength at which clear attenuation of wave velocity is expected, while that at low cyclic stress levels remains unknown.<sup>7</sup> Monitoring of the ultrasonic velocity of granites under cyclic loading has shown a nonlinearly increasing trend of ultrasonic velocity at maximum stress with a slightly decreasing trend in ultrasonic velocity at minimum stress.<sup>18</sup> These studies<sup>7,17,18</sup> based on ultrasonic characteristics contributes to an improved understanding of fatigue-induced damage behavior of natural rocks. However, fatigue-induced damage at low stress levels is typically slight and may not be captured by AE monitoring<sup>17</sup> or traditional ultrasonic velocity testing based on first arrivals.<sup>19,20</sup> This fatigue-induced damage may accumulate with time, causing the ultimate catastrophic failure of the

rock mass under dynamic loading without early indication. Coda wave interferometry (CWI), which is particularly sensitive to minor perturbation based on shear coda waves,<sup>21</sup> represents an alternative means to detect dynamic hazards under repetitive loading.<sup>19</sup>

Coda waves constitute the tail of a seismogram, reflecting multiple scattering in a heterogeneous medium.<sup>22</sup> CWI is an approach to detect temporal changes in a medium by using the scattering medium as an interferometer.<sup>23–25</sup> CWI has been applied in many laboratory and field applications, including monitoring of thermally-induced velocity changes in granite,<sup>26</sup> stress changes in the subsurface,<sup>27,28</sup> temporal changes in volcanic edifices,<sup>29,30</sup> migration of CO<sub>2</sub> plumes during sequestration injection<sup>31</sup> and velocity variations within the subsurface.<sup>32</sup> In comparison to the measurement of direct waves or single scattered waves, one of the great advantages of coda waves is the high sensitivity to only weak perturbation. This is due to the mechanisms of multiple scattering within a heterogeneous medium, which amplifies the subtle internal changes by virtue of the repeated sampling.<sup>20</sup> Thus, CWI represents a potential tool for real-time monitoring of subtle changes in rock properties under small perturbation, which may not be captured by conventional first arrival methods<sup>19,20</sup> or AE methods.<sup>17</sup>

To address the potential of through-volume monitoring of structures in rock we apply coda wave interferometry (CWI) to measure subtle variations in ultrasonic wave-speed as an indicator of fatigue-induced damage over various loading paths. Shale specimens are subjected to both cyclic loading with an increasing stress amplitude for each cycle and to 100 cycles of constant stress amplitude. Changes in the form of the stress-strain curves and the evolution of elastic moduli are used, together with measurements of ultrasonic velocity to characterize fatigue then ultimate failure behavior of the specimens. The utility of first arrivals and time-of-flight analyses versus a full coda analysis are contrasted in defining the emergence of subtle impacts of damage evolutions under the different monotonically-increasing and uniform cyclic loading conditions. This study contributes to a better understanding of stress-sensitive ultrasonic properties and fatigue behavior of shales under cyclic loading, providing guidance in monitoring time-varying stress fields and in predicting time-to-failure of natural and constructed structures in rock.

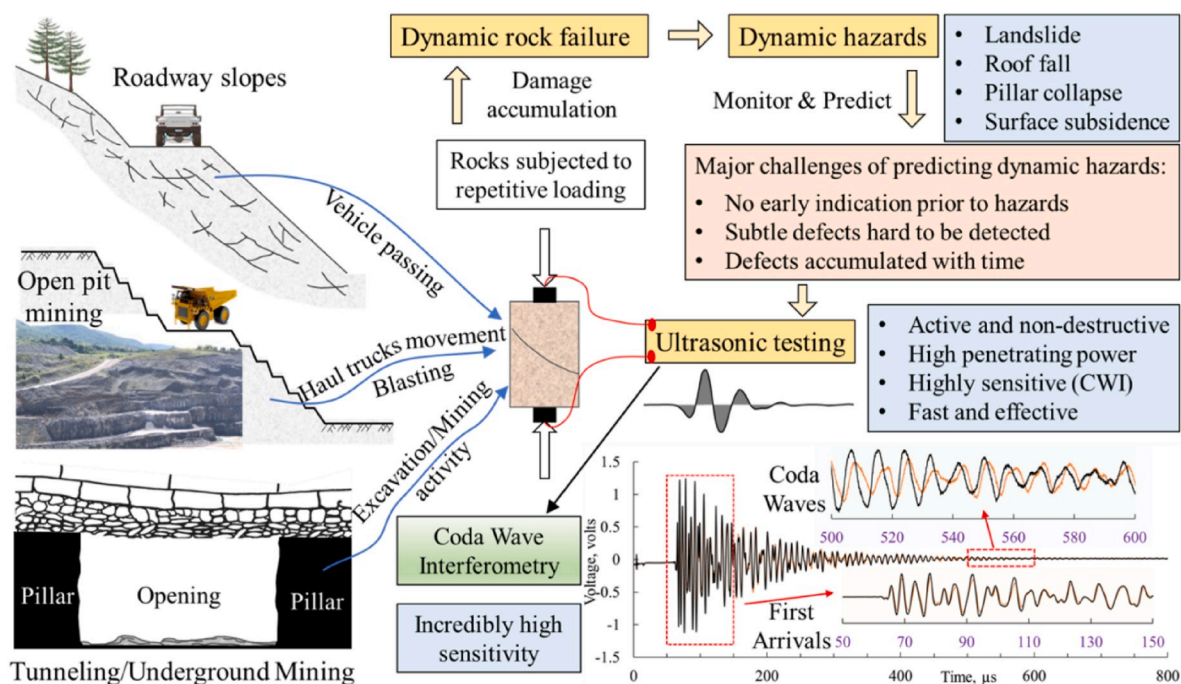


Fig. 1. Schematic representing rock failure under repetitive loading and applications of coda wave interferometry (CWI) to monitor subtle changes in rock structures and hence predict dynamic hazards.

## 2. Experimental details and CWI theory

### 2.1. Shale specimen collection and preparation

Three cylindrical specimens of shale are created from core (Fig. 2) recovered from the immediate roof strata of two underground coal mines in Pennsylvania, USA. Two are from the roof of the Upper Freeport (UF2 and UF3) at a depth of  $\sim 595'$  (180 m) and the third from the roof of the Lower Kittanning (Pen09) at a depth of  $\sim 619'$  (189 m). The shale specimens are drilled in the direction of perpendicular to the strata beddings. The specimens are cut (50 mm diameter and 100 mm long; ASTM D7012) then ground parallel and perpendicular to meet the ASTM D4543 standard before oven-drying for 16 h to remove residual water. The physical parameters classifying the prepared cores are listed in Table 1, which exhibit a uniform dry density of  $2.7 \text{ g/cm}^3$ .

### 2.2. Experimental procedure

We conducted both the real-time mechanical test and the ultrasonic measurement using the servo-hydraulically controlled GCTS Rock Testing System (Fig. 3) (G<sup>3</sup> Center, Pennsylvania State University). Axial linear variable differential transformers (LVDT) were mounted on the support rings to measure the axial strain while the radial LVDT was mounted on a strain-belt wrapped around the specimens for the monitoring of the circumferential strain. The ultrasonic wave velocities were measured using the GCTS ultrasonic system integrating the data acquisition system with signals from a pair of 2-inch platens for pulsing and receiving ultrasonic waveforms. Mounted inside the ultrasonic platens were shear and compression generators/receivers fabricated from piezoelectric ceramics attached in the plane of the flat surface of the ultrasonic platens. Ultrasonic pulses with a central frequency of 200 kHz were excited by the pulsing transducer (attached in the upper platen), and received by the receiving transducer (attached in the lower platen) in the form of an electrical signal that was received and processed by the data acquisition system. The sampling frequency was 20 MHz with the total number of sampled data being 16384. For each ultrasonic waveform 128 traces were stacked to obtain a high signal-to-noise ratio with a high reproducibility. Honey as a coupling gel was smeared evenly on the top and bottom surfaces of the shale specimens. The entire testing suite was conducted in an A/C controlled room ( $\sim 25^\circ\text{C}$ ).

We applied two cyclic loading scenarios to study the fatigue behavior and ultrasonic variation of the three shale specimens along the loading direction. For the UF2 shale specimen (Fig. 4a), the first stage was to load the specimen from pre-stress (0.5 MPa) to 10 MPa at a displacement rate of 0.1 mm/min. This was followed by cyclic loading with continuously increasing maximum stress as: 10 MPa  $\rightarrow$  15 MPa  $\rightarrow$  10 MPa  $\rightarrow$  20 MPa  $\rightarrow$  10 MPa  $\rightarrow$  25 MPa  $\rightarrow$  10 MPa  $\rightarrow$  30 MPa...  $\rightarrow$  failure. The displacement rate was maintained constant at 0.1 mm/min for both loading and unloading with the ultrasonic data collected at both

**Table 1**  
Physical properties of shale specimens.

Specimen	Diameter $D$ , mm	Height $H$ , mm	Dry mass $m$ , g	Density $\rho$ , g/cm <sup>3</sup>
UF2	50.3	100.4	531.0	2.7
UF3	50.4	104.0	558.4	2.7
Pen09	50.3	108.9	576.7	2.7

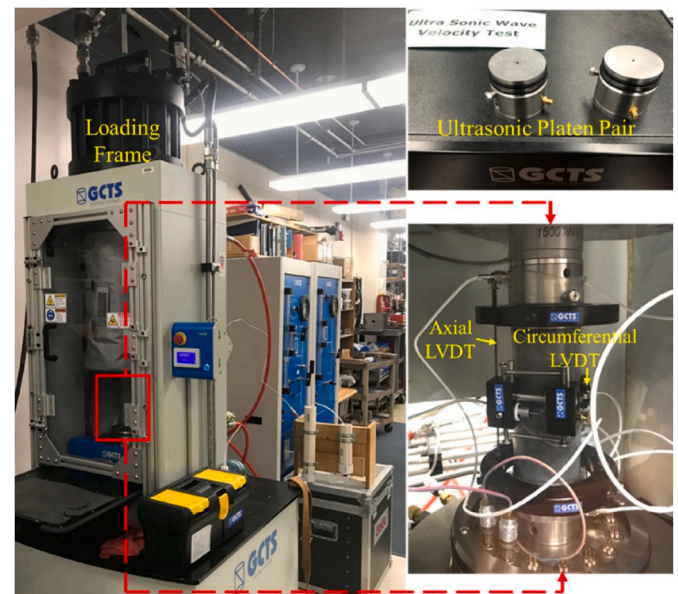


**Fig. 3.** GCTS rock testing system and ultrasonic data acquisition system.

minimum stress (10 MPa) and maximum stresses (15 MPa, 20 MPa, 25 MPa, ...) as marked by red arrows in Fig. 4a. For both the UF3 and Pen09 shale specimens (Fig. 4b and c), the first stage was to load from the pre-stress (0.5 MPa) to 10 MPa again at a displacement rate of 0.1 mm/min. Then, cyclic loading was applied for 100 cycles at a stress rate of 2 MPa/s and at each maximum stress (20 MPa, 30 MPa, 40 MPa, ...). The ultrasonic data were collected at the minimum stress (10 MPa) after every 20-cycles of loading/unloading. For the UF3 shale specimen, the ultrasonic data at each maximum stress condition after the first cycle were also recorded to compare with that for the UF2 shale specimen. In this study, we identify the first scenario loading path as an “increasing-amplitude test” (UF2) and the second loading path a “constant-amplitude test” (UF3 and Pen09). During each ultrasonic recording, the stress was held constant for 1 min, with the collection of 128 traces requiring approximately 50 s.

In this study, we emphasized the fatigue-induced ultrasonic variation



**Fig. 2.** Shale core specimens prepared for the fatigue test under uniaxial cyclic loading.

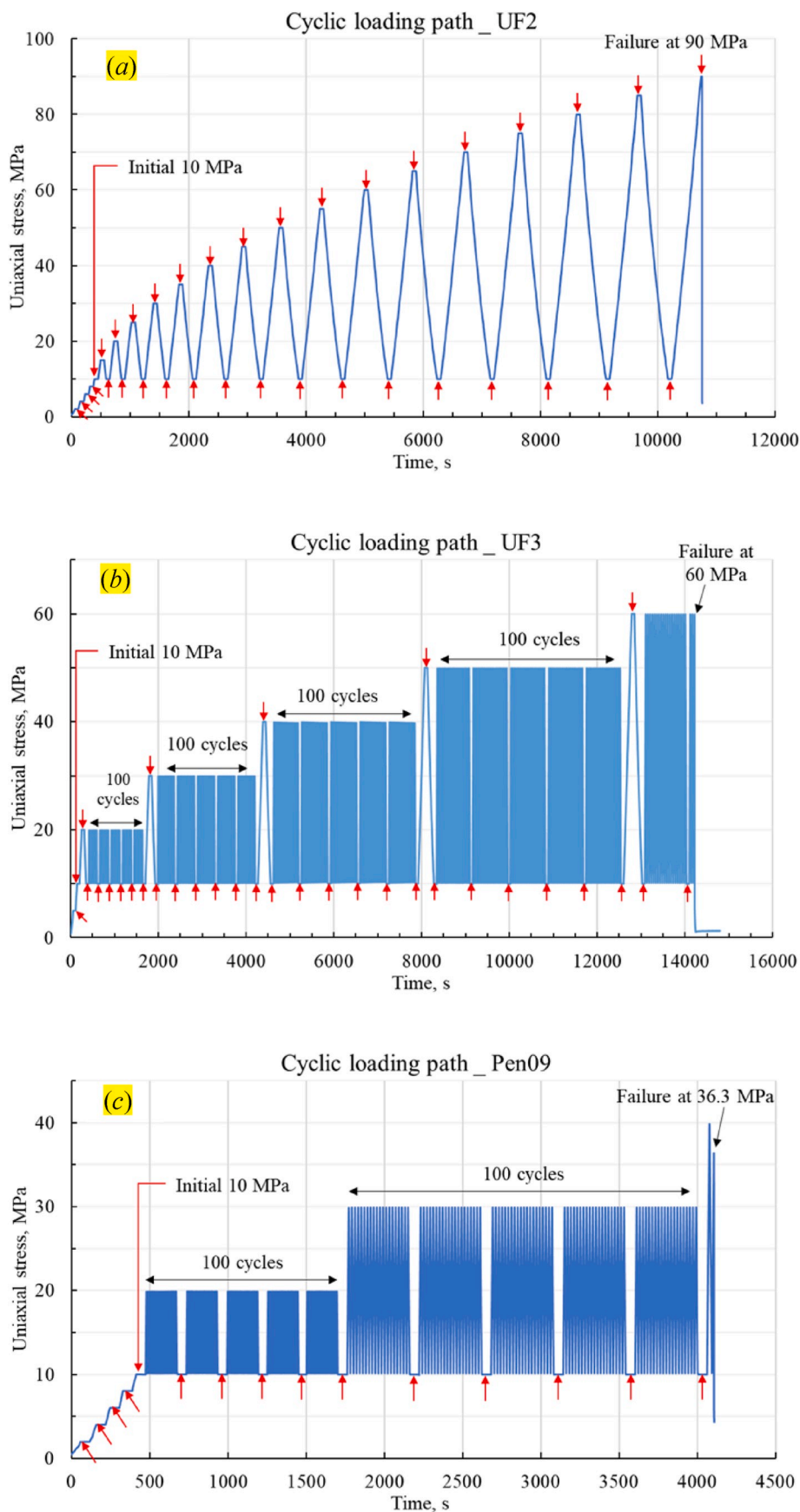


**Fig. 4.** Cyclic loading paths for (a) shale specimen UF2, (b) shale specimen UF3 and (c) shale specimen Pen09. Red arrows mark the stress magnitudes at which ultrasonic data were collected. The initial stress of 10 MPa is also marked as a reference relative to the measurement of ultrasonic velocities at other stress levels and for their intercomparison. (For interpretation of the references to colour in this figure legend, the reader is referred to the Web version of this article.)

under cyclic loading based on a sensitive coda wave interferometry analysis. The ultrasonic data were collected only along the uniaxial loading direction without being monitored in the other two directions which are parallel to the beddings. Stress-induced anisotropic damages, which may occur in transversely anisotropic rocks materials depending on the direction of loading,<sup>33–35</sup> is not analyzed in this study. Since the coda waves can capture and record the entire rock specimen due to multiple scattering, ultrasonic monitoring in the loading direction can capture the structural changes in both parallel and perpendicular cracks which will be discussed in Section 3 (Fig. 20). The subtle changes in microstructures analyzed through CWI can be used for the failure precursor detection in both lab and field scale. In the lab investigation, it is worthwhile to monitor the anisotropic damage in different directions with respect to the loading direction based on multiple transducers<sup>34,36</sup> for the theoretical model refinement, which nevertheless is not the main goal in this study.

### 2.3. CWI and relevant theories

One of the great advantages of using coda waves, compared to direct waves or single scattered waves, is their high sensitivity to weak perturbations in damage. This is primarily due to the longer travelling paths. This enables coda waves to capture subtle time-lapse variations in the medium due to various impacts of stress,<sup>20</sup> humidity,<sup>20</sup> temperature,<sup>23</sup> fluid injection<sup>31</sup> and chemical interaction.<sup>37</sup> Since the multiply scattered coda waves sample the entire medium, CWI samples alteration in bulk properties of that medium, allowing the perturbation of velocity, source location and scatterer locations to be monitored.<sup>21,38</sup> In addition, given repetitive excitation sources, coda waves are highly reproducible in an unperturbed medium and thus provide significant accuracy even when diluted by high levels of background noise.<sup>38</sup> Fig. 5 shows two sample waveforms recorded at an initial stress of 10 MPa and after unloading from 15 MPa, respectively. Note that the time-shift in direct arrivals is almost indistinguishable while the coda waves show an apparent time-shift.

#### 2.3.1. Processing methods

The fundamental feature of CWI is to cross-correlate the coda waves to monitor time-shifts or relative velocity changes. There are two methods for the estimation of relative velocity changes, based on CWI. The seismic doublet method<sup>23–25</sup> measures the time-shift ( $\delta t_i$ ) between two coda waves at several ( $N$ ) non-overlapping time windows. At a

specific time-window ( $t_i-T, t_i+T$ ), the time-shift  $t_s$  of the perturbed trace  $u_p[t]$  relative to the unperturbed trace  $u_u[t]$  maximizes the following cross-correlation coefficient  $CC(t_i, t_s)$  as:

$$CC(t_i, t_s) = \frac{\int_{t_i-T}^{t_i+T} u_u(t)u_p(t+t_s)dt}{\sqrt{\int_{t_i-T}^{t_i+T} u_u^2(t)dt \int_{t_i-T}^{t_i+T} u_p^2(t)dt}} = \max \quad (1)$$

The relative velocity change ( $\delta v/v$ ) is obtained from the mean of all relative time-shifts ( $\delta t_i/t_i$ ):  $\delta v/v = -(1/N)\sum \delta t_i/t_i$ . The doublet method assumes that the time-shift is constant within a specific time-window, which generally is not the case since one may expect a larger time-shift at the tail of a time-window due to its extended wave-travel path. In contrast, the other “stretching” method<sup>39</sup> is to determine the relative velocity change ( $\varepsilon = \delta v/v$ ) as the factor by which the time axis of one trace (perturbed)  $u_p[t]$  is stretched or compressed,  $u_p[t(1\pm\varepsilon)]$ , to best fit the other trace (unperturbed)  $u_u[t]$ . The stretching method does not assume a constant time-shift within a time-window and can be conducted over a much longer time-window in one step. Therefore, the stretching method typically offers a more stable and precise estimation of the relative velocity change (the resolution of the relative velocity change can be as small as  $2 \times 10^{-5}$ ).<sup>40,41</sup> The limitation of the stretching method is that it assumes a linearly increasing time-shift or constant relative velocity change, which may not be valid for media with strongly heterogeneous changes.<sup>39</sup> The relative velocity change  $\delta v/v$  maximizes the cross-correlation coefficient  $CC(\varepsilon)$  of the stretched/compressed perturbed trace  $u_p[t(1\pm\delta v/v)]$  and unperturbed trace  $u_u(t)$  in a time window  $[t_1, t_2]$  as:

$$CC(\varepsilon) = \frac{\int_{t_1}^{t_2} u_p[t(1-\varepsilon)]u_u[t]dt}{\sqrt{\int_{t_1}^{t_2} u_p^2[t(1-\varepsilon)]dt \int_{t_1}^{t_2} u_u^2[t]dt}} = \max \quad (2)$$

where  $\varepsilon$  is the relative velocity change  $\delta v/v$  due to subtle perturbations. The algorithm for the stretching method is as follows: first we assume a small negative value of  $\varepsilon$ , which is chosen by experience or trial-and-error experiments. Then, the stretched perturbed trace is resampled to be cross-correlated with the unperturbed trace. This process is iterated by giving a small increment  $\Delta\varepsilon$  until it comes to  $-\varepsilon$ , thus we can obtain a series of cross-correlation coefficients  $CC(\varepsilon)$  as a function of the relative velocity changes  $\varepsilon$ , whose values are finally determined where the maximal  $CC(\varepsilon)$  is achieved. Fig. 6 shows one of the examples of using the CWI stretching method for the estimation of the relative velocity

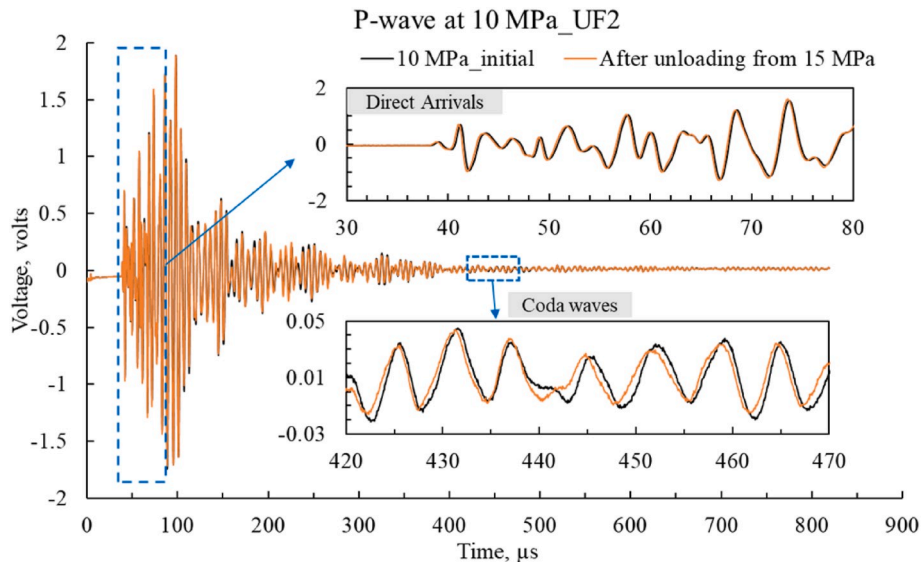


Fig. 5. P-waveforms of shale specimen UF2 recorded at an initial stress of 10 MPa and after unloading from 15 MPa. The two insets show that the time-shift in the direct arrivals are almost indistinguishable while the coda waves show a clear time-shift.

changes based on two signals recorded first at an initial stress of 10 MPa and then after unloading from 15 MPa (also shown in Fig. 5). The “stretched” signal agrees well with the other signal within the selected time-window. In this study, we employ the stretching method to estimate the relative velocity changes between two consecutive recordings based on the step-wise loading sequences as described in Section 2.2.

2.3.2. Relative change in effective velocity and dynamic constants

In an elastic medium, compressive (P) waves usually propagate faster than shear (S) waves. The relative change in the effective velocity, inferred from CWI, is a weighted average of the relative changes of P- and S- wave velocities,<sup>21</sup> expressed as

$$\frac{\delta v}{v} \approx \frac{v_s^3}{2v_p^3 + v_s^3} \frac{\delta v_p}{v_p} + \frac{2v_p^3}{2v_p^3 + v_s^3} \frac{\delta v_s}{v_s} \quad (3)$$

where  $v_p$  and  $v_s$  are P- and S- wave velocities, respectively; and  $\delta v_p$  and  $\delta v_s$  are relative changes in the P- and S- wave velocities, respectively. For a Poisson medium where  $v_p = \sqrt{3}v_s$ , the above relation can be simplified as<sup>21</sup>

$$\frac{\delta v}{v} \approx 0.09 \frac{\delta v_p}{v_p} + 0.91 \frac{\delta v_s}{v_s} \quad (4)$$

This relation shows that the relative change in the effective velocity inferred from CWI depends much more strongly on the perturbation in the S-wave velocity. Theoretically, CWI analysis based on S-coda waves can be used as a sentinel for subtle changes in a medium.

Dynamic elastic constants can also be determined by the P- and S-wave velocities. Assuming that a medium is elastic, homogeneous, and isotropic, then the dynamic elastic modulus  $E$  and Poisson’s ratio  $\nu$  can be expressed as

$$E = \frac{\rho v_s^2 (3v_p^2 - 4v_s^2)}{v_p^2 - v_s^2} \quad (5)$$

$$\nu = \frac{v_p^2 - 2v_s^2}{2(v_p^2 - v_s^2)} \quad (6)$$

where  $\rho$  is the density of the medium.

3. Results and discussion

3.1. Rock static mechanical properties under repetitive loading-unloading

3.1.1. Stress-strain curves with repetitive loading and unloading conditions

The stress-strain curves for the three shale specimens cyclically-loaded in this study are shown in Figs. 7 and 8, exhibiting an apparent hysteresis under the cyclic loading. Shale specimen UF2 in the

“increasing-amplitude test” failed at a peak stress of 90 MPa (Fig. 7) when ultrasonic data were being collected. Under the increasing-amplitude test, the relation between the peak stress and monotonic strength varies depending on the rock type, loading rate and loading pattern.<sup>3</sup> Rock failure may occur at an applied peak stress close to,<sup>13</sup> lower than<sup>42</sup> or high than<sup>43</sup> the monotonic strength. Under the constant-amplitude test shown in Fig. 8, the failure behaviors of the two tested shale specimens are different. Specimen UF3 started to fail at 56 MPa during the 23rd cycle of loading (cyclic maximum stress being 60 MPa), resulting from the irreversible fatigue damage accumulated under repeated cycles. For specimen Pen09, failure began at 36 MPa during the 1st cycle of loading (cyclic maximum stress being 40 MPa), indicating that an increase of applied stress amplitude can induce primary yield/damage and then trigger the failure. However, it is still not clear how failure of specimen Pen09 is related to the number of repeated load cycles at previous maximum stress levels (30 MPa) based on the stress-strain relations. The role of the cumulative number of cycles under various maximum stress levels will be discussed in Section 3.2 in terms of the ultrasonic evolution. From Fig. 8, both shale specimens failed after an abrupt increase in radial strain at the stress level close to the maximum stress. Consistently, after the initiation of failure and prior to the catastrophic failure, both specimens sustained slightly higher stresses than the failure initiation stress. As a matter of fact, sample Pen09 survived the entire 1st cycle of loading/unloading (a maximum stress of 40 MPa) and failed at 36 MPa during the 2nd cycle of the loading process as shown in Fig. 8. Under the constant-amplitude test,

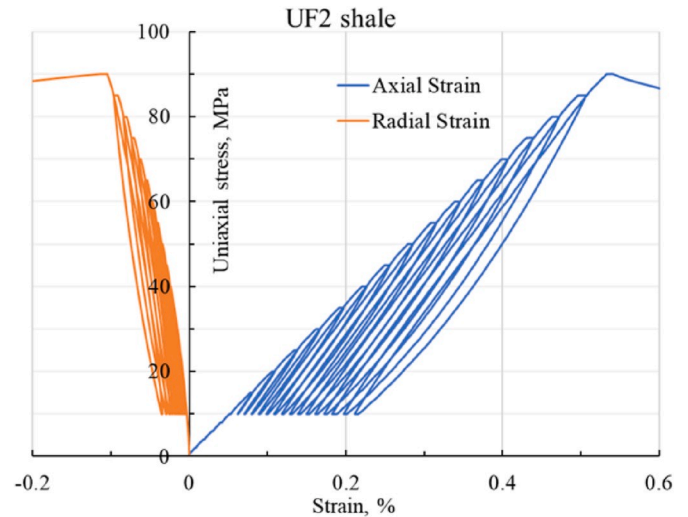


Fig. 7. Stress-strain relation of shale specimen UF2 in the “increasing-amplitude test.”

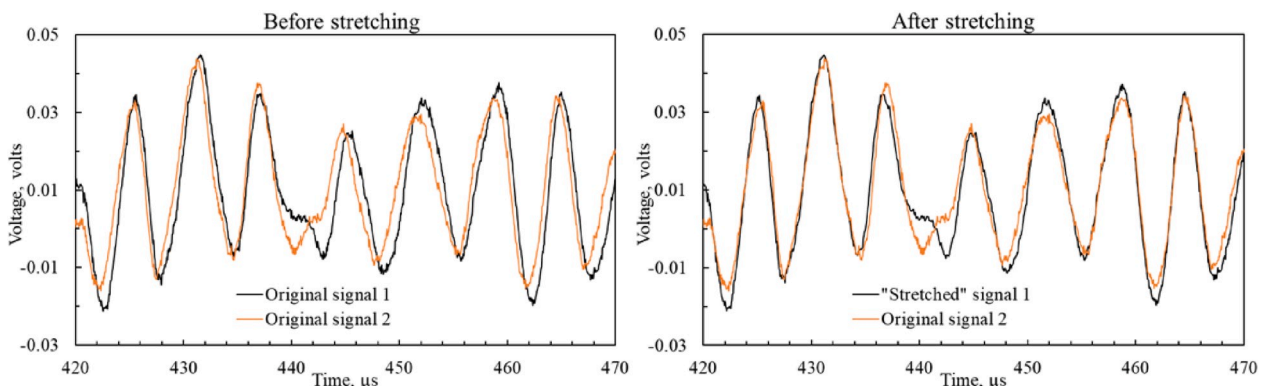


Fig. 6. CWI stretching method showing the match between two coda waves; the relative velocity change (stretching factor) is estimated as 5.3e-4.

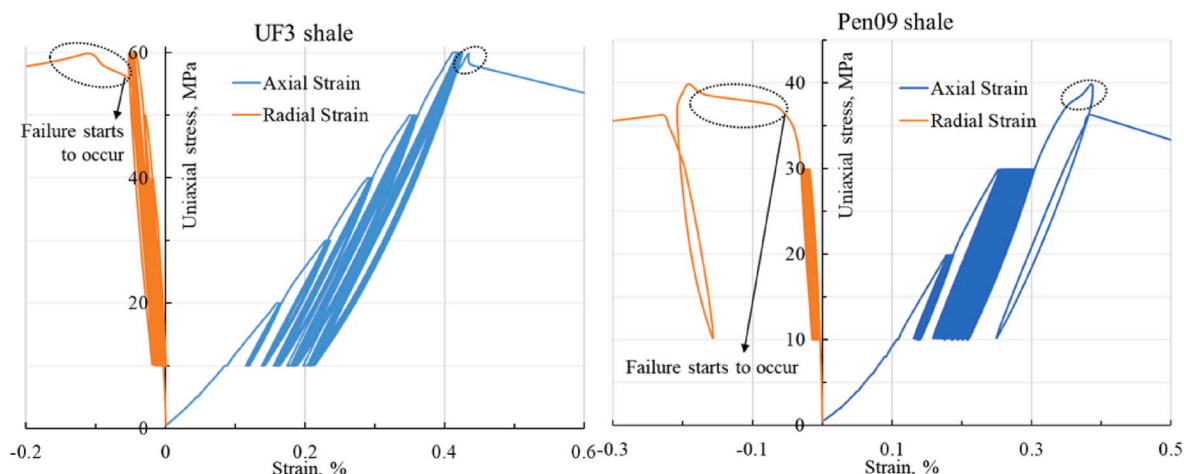


Fig. 8. Stress-strain relations of shale specimens UF3 and Pen09 under “constant-amplitude tests” (100 cycles at each maximum stress).

failure is expected to occur at a maximum cyclic stress that is lower than the estimated monotonic strength due to the weakening effect induced by the repetitive cycles.<sup>44</sup> However, for a specific rock, it is challenging to identify the relation between its strength and the maximum cyclic stress since both parameters are needed to fail the single rock specimen.

### 3.1.2. Elastic constants of tested rock specimens

Monitoring the evolution of elastic modulus as an indicator damage and reduction in strength has been previously reported as following either decreasing<sup>14,42,45</sup> or increasing trends<sup>46</sup> under “increasing-amplitude” loading and mostly as absent degradation under “constant-amplitude” tests.<sup>7,14,44</sup> Evolution of elastic moduli for the three specimens studied in this work is shown in Fig. 9 and Fig. 10. The elastic modulus during unloading was slightly larger than that during the loading process, suggesting a hardening effect due to the cyclic compression. This hardening effect has been primarily attributed to yielding or to the irreversible compaction of micro-fractures,<sup>47</sup> corresponding to the stress-strain hysteresis as shown in Figs. 7 and 8. Under the loading of the “increasing-amplitude” test, as shown in Fig. 9, the hardening effect remains almost constant with an increase in the maximum stress. Poisson’s ratio of shale UF2 shown in Fig. 9 (b) continues to increase with an increase in the maximum stress, which may be attributed to the fatigue-induced damages under cycles of increasing stress amplitude. However, based on the evolution of the Poisson’s ratio, no critical limit at earlier stage can be identified to serve as a failure indicator where the induced microcracks start to dominate over the microcracks closure. This critical limit, however, can be recognize by the decrease of the wave velocity based on CWI as shown in Fig. 15 in Section 3.2.2. Thus, the CWI is a superior technique for detecting the

micro-structure modification as the failure precursor.

Under constant-amplitude loading (Fig. 10), the modulus showed a slight increase with the increase in number of cycles at low stress levels but showed almost no change with number of cycles at high stress levels. From Fig. 10, the hardening effect for both shale samples UF3 and Pen09 became progressively more obvious with an increase in the maximum stress. This may result from more progressive yielding and irreversible compaction of micro-fractures at higher stress levels. However, there is still no direct mechanistic linkage of how the evolution of elastic moduli are related to the failure behavior of the three shales. Thus, the monitoring of elastic modulus may not be a robust indicator of damage in predicting ultimate rock failure. Evolution of Poisson’s ratio of shale samples UF3 and Pen09 under “constant-amplitude test” as shown in Fig. 10 (c) & (d) also exhibits an increasing trend with the increased stress. One can also observe from Fig. 10 (c) & (d) that the Poisson’s ratio for the two shales is free from the effect of cyclic numbers at low maximum stress levels, while shows an increasing trend with cyclic numbers at high maximum stress levels. This indicates an accumulation of fatigue-induced damage at high maximum stress levels and eventually trigger the rock failure. In this point, the evolution of Poisson’s ratio is a good indicator of fatigue-induced damages under constant-amplitude loading. However, it is quite challenging to obtain the evolution of Poisson’s ratio in the field based on stress-strain curves. A more robust and non-destructive means is still required for the recognition of the fatigue-induced damages of the rock materials.

### 3.2. Evolution of ultrasonic velocity

In this section, we discuss the stress-dependent variation of

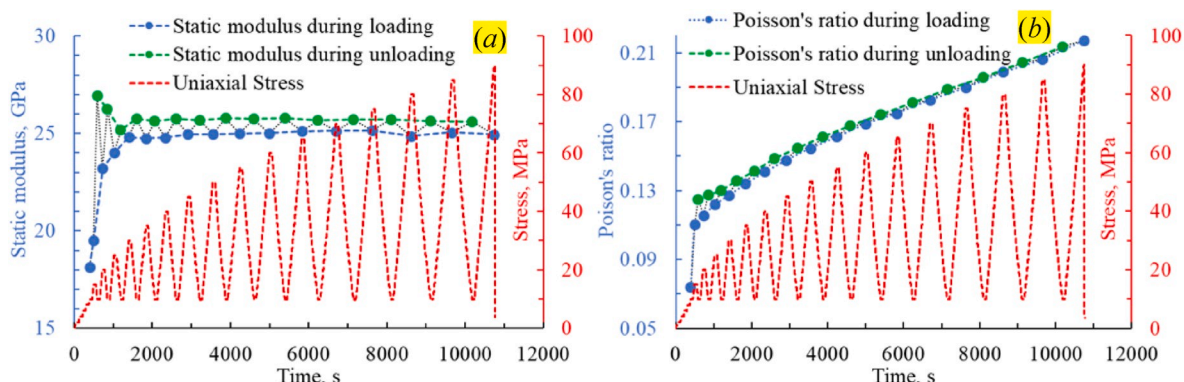


Fig. 9. Evolution of (a) static modulus and (b) Poisson’s ratio of shale specimen UF2 under the loading of an “increasing-amplitude test.”

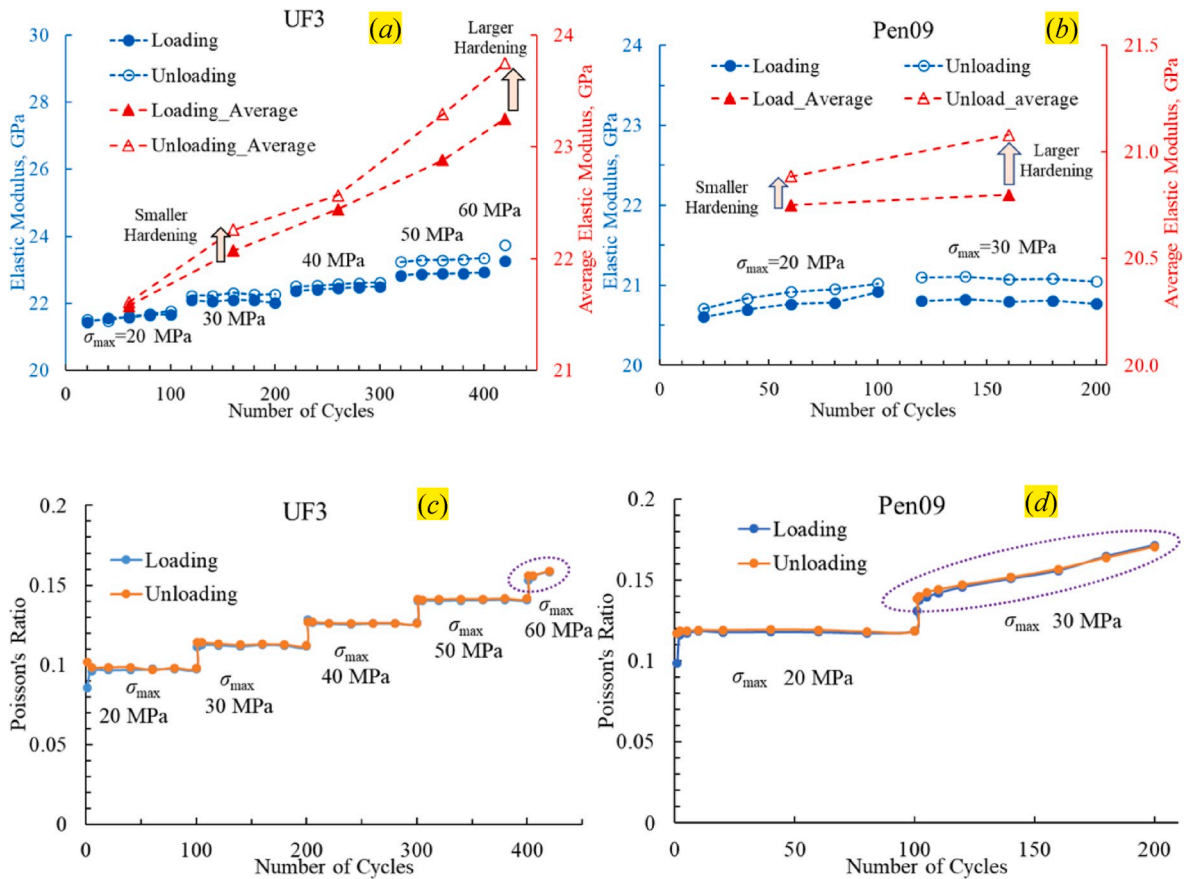


Fig. 10. Evolution of elastic modulus of (a) shale sample UF3 and (b) Pen09; and evolution of Poisson's ratio of UF3 (c) and Pen09 (d) under the loading of the "constant-amplitude test" (100 cycles at each maximum stress).

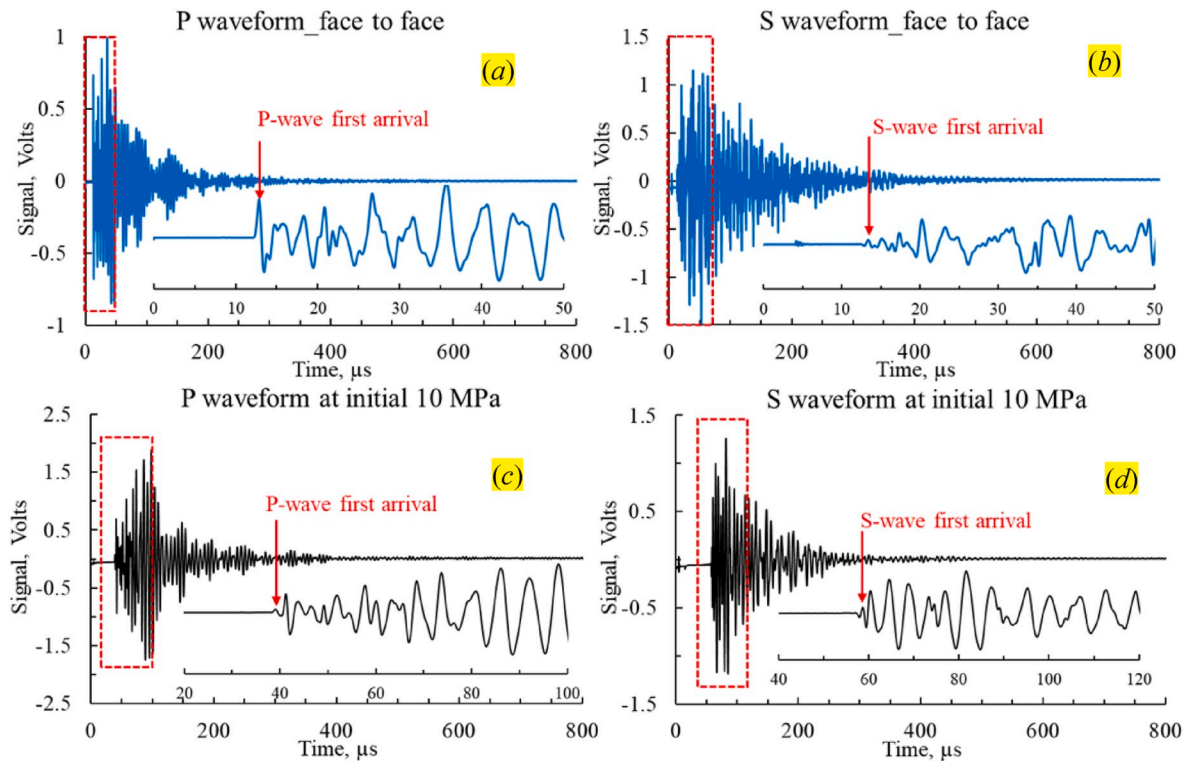


Fig. 11. First arrival picks for the calculation of ultrasonic velocities at an initial stress of 10 MPa (UF2 shale): (a) P-waveform and (b) S-waveform obtained by face-to-face measurement without specimen between the two transducers; (c) P-waveform and (d) S-waveform of specimen UF2 recorded at the initial stress of 10 MPa.

ultrasonic velocities at different stress amplitudes (Section 3.2.1) and fatigue-induced variation in ultrasonic velocities at 10 MPa with different loading paths (Section 3.2.2). The estimation of the ultrasonic velocities at different stress amplitudes was based on the first arrival method through measuring time-shifts between the recording at an initial stress of 10 MPa (as a reference) and that at other stresses. In this instance, first arrival method was applied instead of CWI since CWI may perform poorly at high stress levels where the rock structure and hence waveforms change dramatically.<sup>38,48,49</sup> The estimation of the ultrasonic velocities at 10 MPa for different loading paths was based on the CWI stretching method through measuring the relative velocity changes between one trace and the next adjacent trace as detailed in Section 2.3.1. This moving-reference method has also been adopted in other studies.<sup>38,48,49</sup> In this case, ultrasonic velocity at the initial stress of 10 MPa was also calculated as an initial reference.

Fig. 11 (a) and (b) show the picking of first arrivals for the face-to-face measurement (without putting the specimens between the two transducer platens). Fig. 11 (c) and (d) show the picking of first arrivals for shale specimen UF2 at the initial stress of 10 MPa. The time-of-flight ( $\Delta t$ ) is the difference between the first arrival of face-to-face measurement and the first arrival of shale UF2. The P- and S- wave velocities ( $V_{P/S}$ ) were calculated using the length of the specimen ( $L$ ) and time-of-flight ( $\Delta t$ ):  $V_{P/S} = L/\Delta t$ . Table 2 shows the ultrasonic velocities for the three tested shale specimens and their corresponding dynamic elastic constants (Eq. (5) and (6)). The dynamic Young's moduli were  $\sim 30$  GPa, larger than the static Young's moduli (Figs. 9 and 10). This possibly results from the difference in strain amplitude due to the nonlinear deformation of the rock specimen.<sup>50,51</sup>

### 3.2.1. Stress-dependent changes in ultrasonic velocities

Fig. 12 and Fig. 13 show the first arrivals of the P- and S- waveforms at different maximum stresses for samples UF2 and UF3, respectively. These exhibit negative time-shifts with an increase in the stress. Based on the time-shifts between the first arrival at an initial stress of 10 MPa and that at other stresses, the P- and S- wave velocities (Fig. 14) for samples UF2 and UF3 were calculated and corrected by considering the effect of deformation – this effect was negligible at low stresses but non-negligible at high stresses. From Fig. 14, the P- and S- wave velocities show an overall increasing trend with increased stress for both tested specimens. This can result from the increase in rock stiffness and rock densification at relatively high stresses due to the closure of micro-fractures subjected to uniaxial compaction. From Fig. 14, S-wave velocity reached a plateau and slightly decreased when the applied stress exceeded 80 MPa, indicating that stress-induced damage occurs and impedes the S-waves at relatively high stresses ( $>80$  MPa). The stage at which S-wave velocity reaches a peak has been closely associated with the volumetric change from compaction to dilation in shale specimens.<sup>52</sup> However, our results demonstrated that the peak S-wave velocity of sample UF2 occurred before the onset of volumetric dilatancy when the specimen had already failed (Fig. 7).

Interestingly, for sample UF3 under constant-amplitude loading, both P- and S- wave velocities continued to increase in a roughly linear pattern from 10 MPa to 60 MPa, indicating that there were no major changes in damage prior to the first cycle of loading to 60 MPa. However, sample UF3 failed after 23 cycles of loading/unloading at a

maximum stress of 60 MPa, suggesting that fatigue-induced damage accumulated progressively with increase in cycles and eventually triggered the failure. Also note that specimens UF2 and UF3 were cut from the same intact block (Fig. 2) and should have similar strengths. That specimen UF2 failed at a maximum stress of 60 MPa ( $<90$  MPa) also supported, to some extent if not considering the heterogeneity, the point that shale failure could be triggered at a maximum stress smaller than the peak strength due to the accumulation of fatigue-induced damage with the number of cycles. In this sense, a higher ultrasonic velocity at higher maximum stress does not necessarily indicate a damage-free rock specimen due to the lack of a comparison at the same stress level. The increasing trend in ultrasonic velocities with maximum stresses cannot reflect subtle fatigue damage of the shale specimens, which can be represented through the decrease in ultrasonic velocities monitored at 10 MPa, as discussed in the following section.

### 3.2.2. Fatigue-induced variation in ultrasonic velocities

The CWI stretching method using a moving-reference frame was employed to probe the subtle changes in P- and S- wave velocities of the three specimens at 10 MPa under different loading conditions. Evolution of P- and S- wave velocities at 10 MPa, under different loading-unloading conditions, were plotted in Fig. 15 for specimen UF2, Fig. 16 for specimen UF3, and Fig. 17 for specimen Pen09. For the “increasing-amplitude” test (UF2) and constant-amplitude test (UF3 and Pen09), cyclic loading-unloading causes an initial increase in the ultrasonic velocities, followed by a descending trend prior to failure. The propagation of ultrasonic waves is influenced by the counteracting effects of micro-fracture closure and fatigue-induced microfractures, depending on the stress level and the loading path. For specimen UF2 under increasing-stress-amplitudes (Fig. 15), the increase of P- and S- wave velocities in the early stages was primarily induced by the irreversible closure of micro-fractures due to cyclic compression, which was also the major cause of the early stage stress-strain hysteresis. The decreasing trend in P- and S- wave velocities at the later stage was mainly induced by fatigue-induced microfractures under the relatively high-stress cycles. For specimen UF3 under the “constant-amplitude” test (Fig. 16), the P- and S- wave velocities (green dash line) collected after the 1st cycle of unloading from each maximum stress show a similar trend to specimen UF2 under the increasing-amplitude test. At the same maximum stress levels, less than or equal to 50 MPa, an increase in load cycles tends to enhance both P- and S-wave velocities due to an irreversible compaction of micro-fractures, while at the maximum stress level of 60 MPa, both P- and S- wave velocities decrease dramatically after 20 cycles of loading and unloading. This was followed by failure occurring on the 23rd cycle of loading/unloading, indicating that cyclic damage accumulated with increasing cycles and triggered the failures. Similar phenomena occur in specimen Pen09 under the constant-amplitude test. At a maximum stress amplitude of 30 MPa, both P- and S- wave velocities decreased dramatically prior to failure, which occurred on the 1st cycle of the new maximum stress level (40 MPa). The dramatic decrease of P- and S- wave velocities with respect to loading cycle number at the maximum stress of 30 MPa shows direct evidence that fatigue-induced damage indeed occurred under this cyclic stress conditions. However, this fatigue-induced damage can be detected neither from the stress-strain curves nor the evolution of the elastic moduli as previously discussed in Section 3.1.

As discussed previously, under either increasing-amplitude or constant-amplitude loading conditions, the P- and S- wave velocities tend to increase at low-stress levels and tend to decrease at high-stress-level cycles (Figs. 15–17). The descending trend of the P- and S- wave velocities with respect to either maximum stress or number of cycles reflects fatigue-induced damage under cyclic loading. Note that CWI based on the stretching method estimates the relative changes in velocity to a resolution of  $\sim 2 \times 10^{-5}$ .<sup>40,41,53</sup> Such subtle microstructural changes, illuminated by the high sensitivity CWI technique, may not be captured by conventional stress-strain curves and even acoustic

**Table 2**

P- and S- wave velocities at an initial stress of 10 MPa and the corresponding dynamic elastic constants for the three shale specimens.

Shale specimen	Ultrasonic velocities		Dynamic elastic constants	
	P-wave velocity, m/s	S-wave velocity, m/s	Young's modulus, GPa	Poisson's ratio
UF2	3704.2	2175.8	31.2	0.24
UF3	3523.2	2168.2	29.9	0.20
Pen09	3879.5	2170.4	31.9	0.27

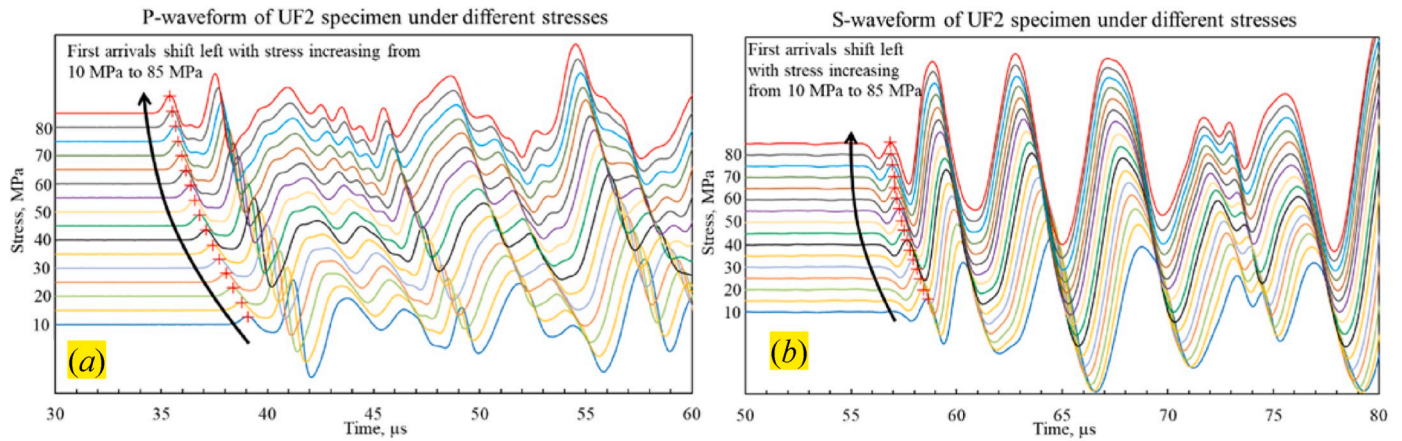


Fig. 12. First arrivals of (a) P-waveforms and (b) S-waveforms of sample UF2 under different stresses from 10 MPa to 85 MPa.

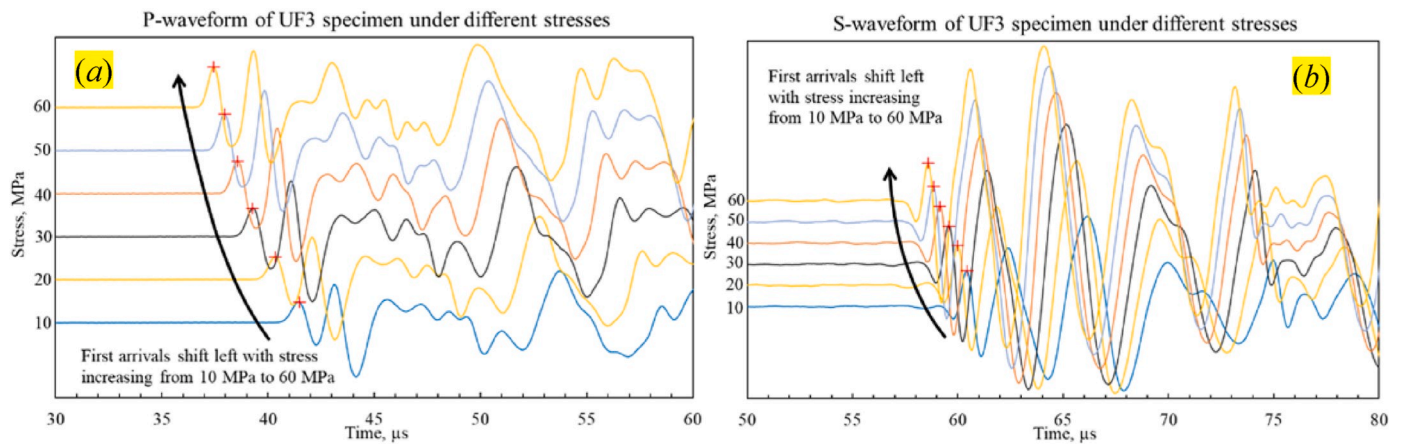


Fig. 13. First arrivals of (a) P waveforms and (b) S waveforms of sample UF3 under different stresses from 10 MPa to 60 MPa.

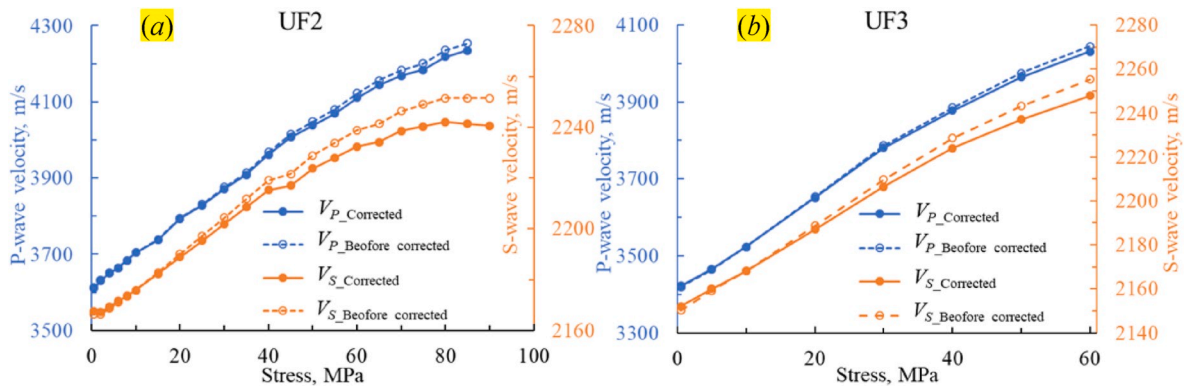


Fig. 14. Evolution of ultrasonic velocity at maximum stresses for (a) shale sample UF2 and (b) specimen UF3 based on first arrivals. Ultrasonic velocities were corrected considering deformation-induced changes in rock lengths at different stresses.

emission (AE) methods due to reality of a detection threshold in the post-processing of the AE signals.<sup>54</sup> In this sense, CWI is an excellent tool to discern subtle changes in ultrasonic velocity and fatigue behavior under repetitive loading conditions. From Figs. 15 to 17, it is apparent that the subtle changes in the shale were more sensitive to S-wave than to P-wave monitoring. Snieder [2002] also shows that CWI velocity change is dominated by the propagation and scattering of S waves after multiple scattering, especially for Poisson media including natural rocks.<sup>21</sup> Dramatic changes in S- wave velocity are strongly associated with fatigue-induced damage and failure behavior, providing a means to

detect hazard precursors under dynamic loading.

### 3.3. Coda waves versus first arrivals

Despite the descending trend of ultrasonic velocities in the later stages for specimen UF2, based on CWI (marked by the black dashed elliptical line in Fig. 15), corresponding to the right shifting of the coda waves at high-stress cycles (Fig. 18), the P- and S- wave velocities apparently increase, based on first arrivals (Fig. 19). This phenomenon also occurred for samples UF3 and Pen09 at high-stresses for the

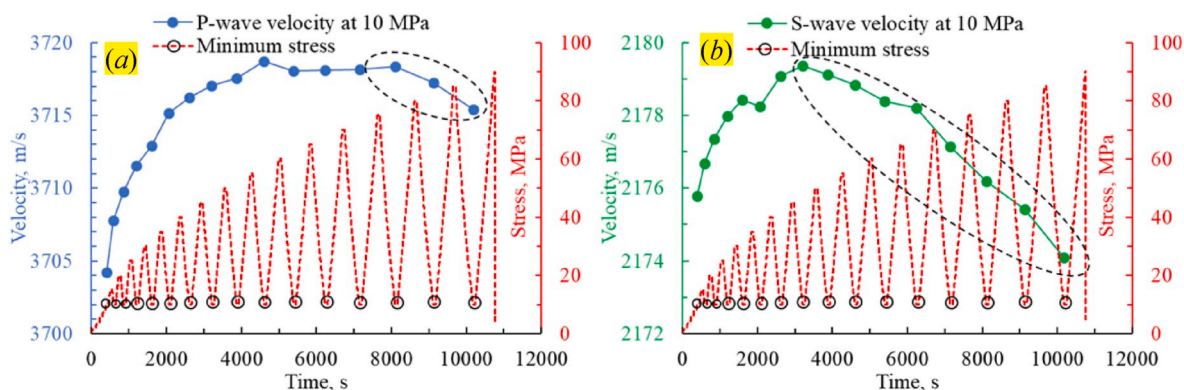


Fig. 15. Evolution of (a) P- wave velocity and (b) S- wave velocity of sample UF2 at 10 MPa for the “increasing-amplitude” test.

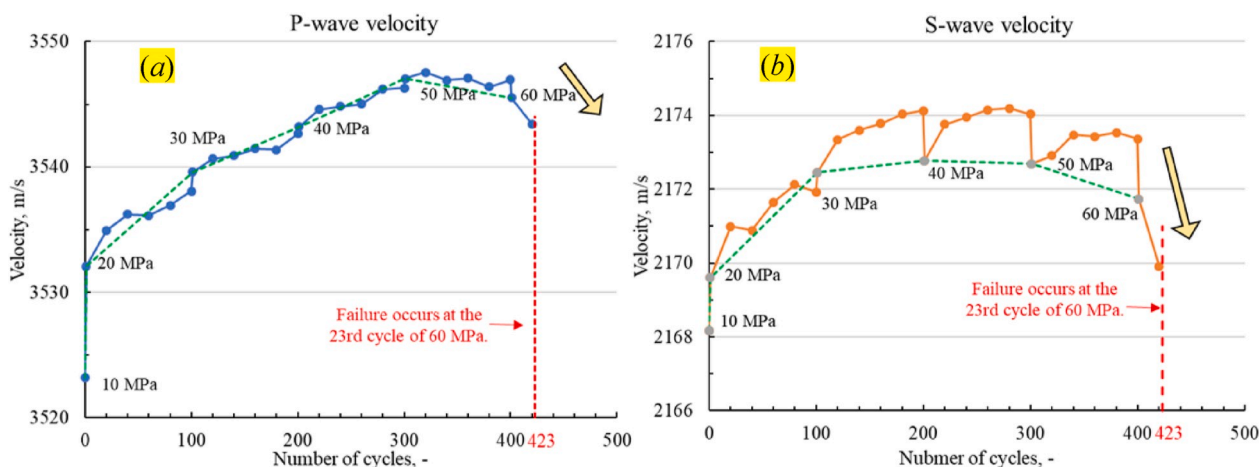


Fig. 16. Evolution of (a) P- wave velocity and (b) S- wave velocity of sample UF3 at 10 MPa with respect to cycle number for different maximum stress cycles (20 MPa, 30 MPa, 40 MPa, 50 MPa, 60 MPa).

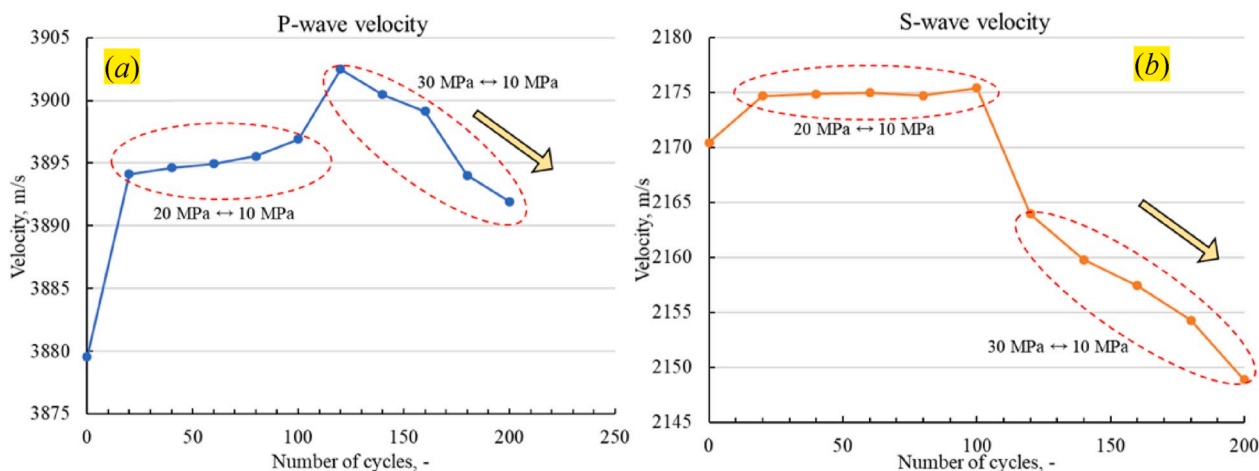


Fig. 17. Evolution of (a) P- wave velocity and (b) S- wave velocity of sample Pen09 at 10 MPa with respect to cycle number at different maximum stress cycles (20 MPa, 30 MPa).

constant-amplitude test. It seems that the inconsistency between coda wave and first arrivals analyses are contradictory at high-stresses - this questions the previous analyses based solely on coda waves. As mentioned previously, the multiply scattered coda waves sample the perturbation in the entire medium, while first arrivals only sample the perturbation once (or not at all) on the ray-path - reflecting the nearest travelling path of the specimens. This makes coda waves sensitive to

trivial changes in microstructure which may not be visible to first arrivals. Specifically, the inconsistency between coda waves and first arrivals can be explained as in Fig. 20. Under cyclic loading-unloading, ultrasonic variations in terms of the arriving time of first arrivals and coda waves are controlled by the opposing effects of irreversible closure of the micro-fractures and fatigue-induced generation of micro-fractures. At low-stress and intermediate-stress cycles, the irreversible

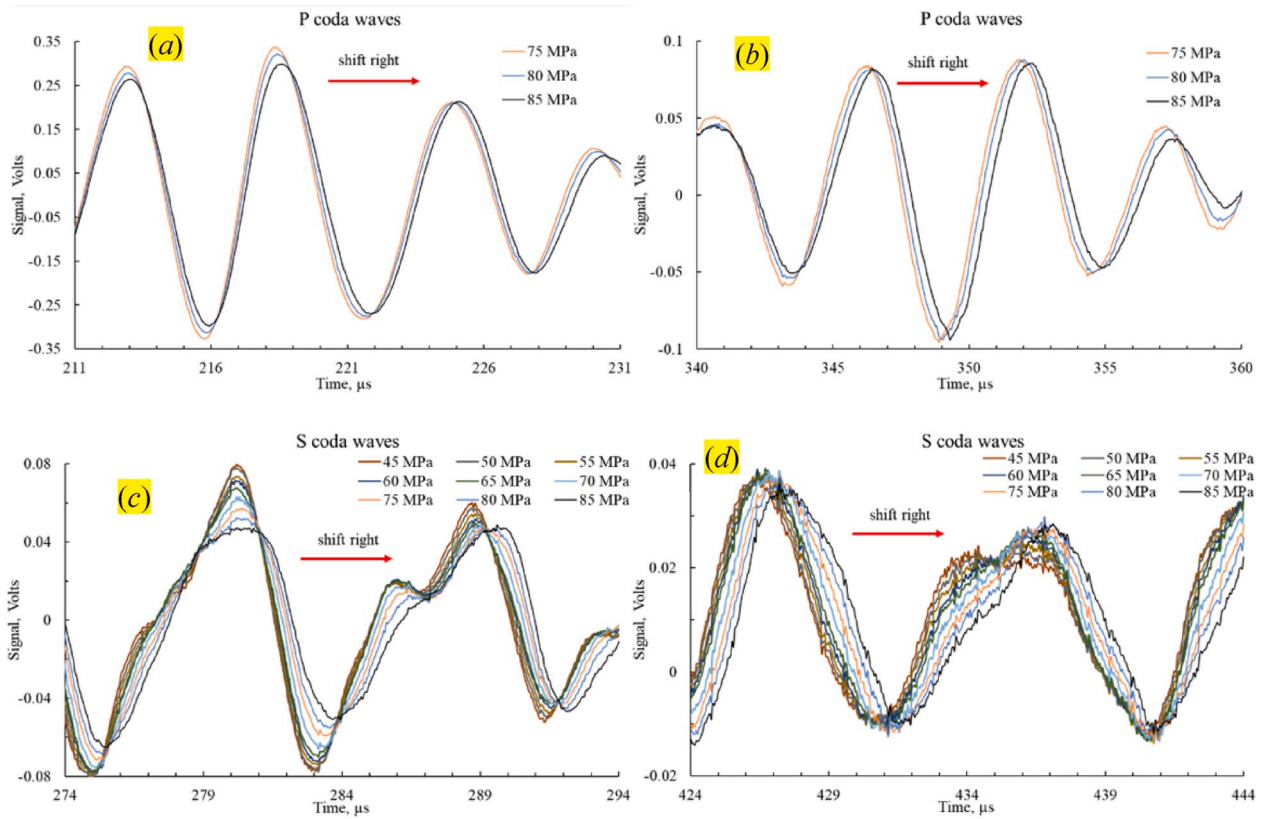


Fig. 18. P- and S- waveforms of specimen UF2 under an “increasing-amplitude” test showing coda waves shifting right with stress at high maximum stress cycles. (a) P- coda waves at time window of (211 μs, 231 μs); (b) P- coda waves at time window of (340 μs, 360 μs); (c) S- coda waves at time window of (274 μs, 294 μs); (d) S- coda waves at time window of (424 μs, 444 μs).

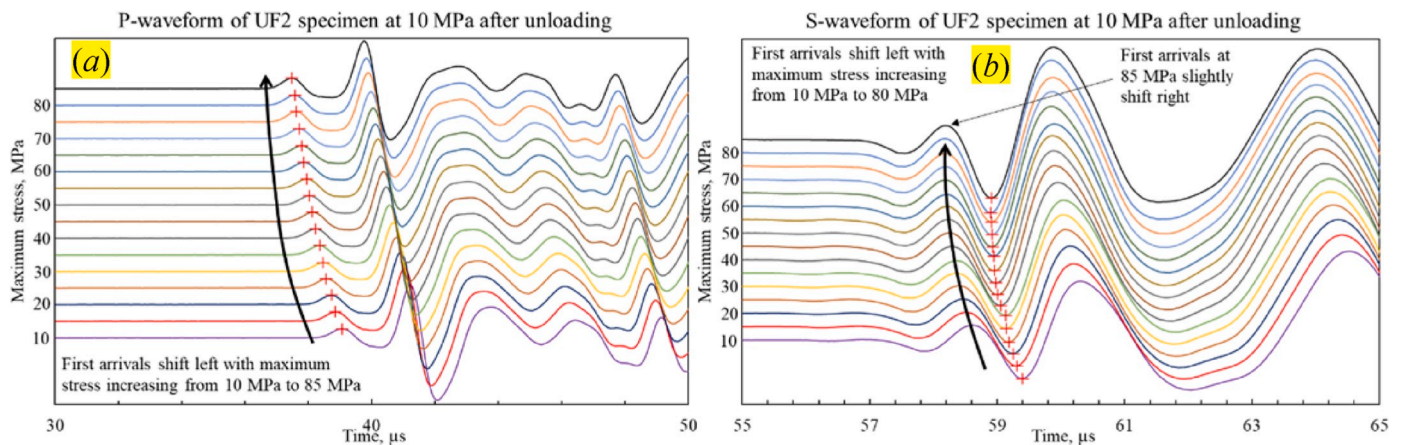
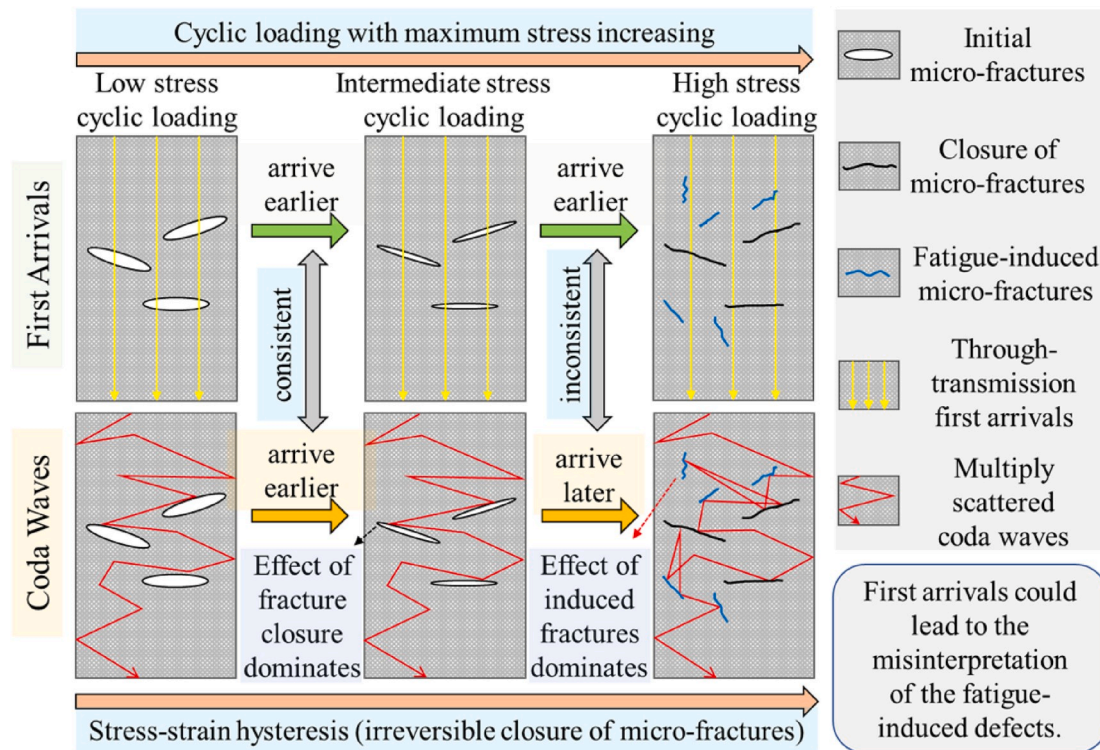


Fig. 19. (a) P- waveforms and (b) S- waveforms of specimen UF2 under an “increasing-amplitude” test. The first arrivals shift left for peak stress cycles from 10 MPa to 85 MPa.

closure of the micro-fractures play a dominant role in decreasing the travel time of both first arrivals and coda waves. This leads to an increase in the ultrasonic velocity based on both first arrivals and coda waves. At high-stress cycles, however, fatigue-induced microfractures, induced either by high stress amplitudes or large numbers of cycles, tend to increase the travel time of the multiply scattered coda waves as is shown in Fig. 20. There are possibly two types of perturbations due to the involvement of the fatigue-induced micro-fractures<sup>21,38</sup>. One of the perturbations is to add new scatterers in the shale specimen, causing more complex multiple scattering and hence lengthening the travel paths of the coda waves. The other is the perturbation in velocity, the

degradation of which is due to the introduction of fresh fractures and leads to an increase in the travel time of the coda waves. Both these perturbations tend to cause positive time-shifts in the coda waves as maximum stress increases. Since first arrivals only sample the perturbation once, or not at all, certain fatigue-induced microfractures may not be sampled by the first arrivals. To the contrary, the irreversible closure of the micro-fractures tends to shorten the nearest travelling path or enhance the wave velocity. This would result in an overall overestimation of the ultrasonic velocities at high-stress levels based on first arrivals. In other words, first arrivals are free from the effect of fatigue-induced micro-fractures to some extent, unless major fractures



**Fig. 20.** Schematic of first arrivals (yellow) reflecting the nearest travel path and coda waves (red) reflecting multiple scattering under different cyclic loading stresses. First arrivals sample the defects either singly or not at all while coda waves sample the entire medium multiple times. (For interpretation of the references to colour in this figure legend, the reader is referred to the Web version of this article.)

are induced, at which stage the shale is primed for failure or has already failed. In this sense, conventional first arrival methods may result in misleading interpretations of fatigue-induced internal damage and thus may not be a useful tool to detect precursory rock failure under cyclic loading.

### 3.4. Fatigue-induced changes in effective velocities and dynamic constants

According to the theory of elastic wave propagation, dynamic elastic constants were calculated based on P- and S- wave velocities at a stress level of 10 MPa, according to Eqs. (5) and (6), while the relative changes in the effective velocity inferred from CWI were estimated through the weighted average of the perturbations in the P- and S- wave velocities at a stress level of 10 MPa, according to Eq. (4). The results are shown in Figs. 21–23. The dynamic Poisson’s ratios overall increased as shown in Figs. 21–23 (a), which is consistent with the evolution of the static

Poisson’s ratio shown in Fig. 9 (b). This is also consistent with most studies that Poisson’s ratio increases with uniaxial stress levels, corresponding to dilative behavior of rocks.<sup>3,45,55</sup> The dynamic Young’s modulus of shale UF2 (Fig. 21 (a)) shows an increase at low-stress cycles (<50 MPa) and decreases at high-stress cycles (>50 MPa). The peak value of the dynamic modulus occurred in the stress cycle (50 MPa) at which the counteracting effects of irreversible fracture closure and fatigue-induced fracture initiation led to the maximum rock hardening. This critical stress cycle (50 MPa) is well represented by the relative changes in the effective velocity as shown in Fig. 21 (b). At low-stress levels (<50 MPa), the increase of the effective velocity corresponded to the increase of the dynamic modulus; at high-stress levels (>50 MPa), the decrease in the effective velocity corresponded to the decrease in the dynamic modulus. Similar phenomena were also observed for samples UF3 and Pen09 under constant-amplitude tests where at high-stress cycles the decreases in the dynamic moduli correspond to the decrease

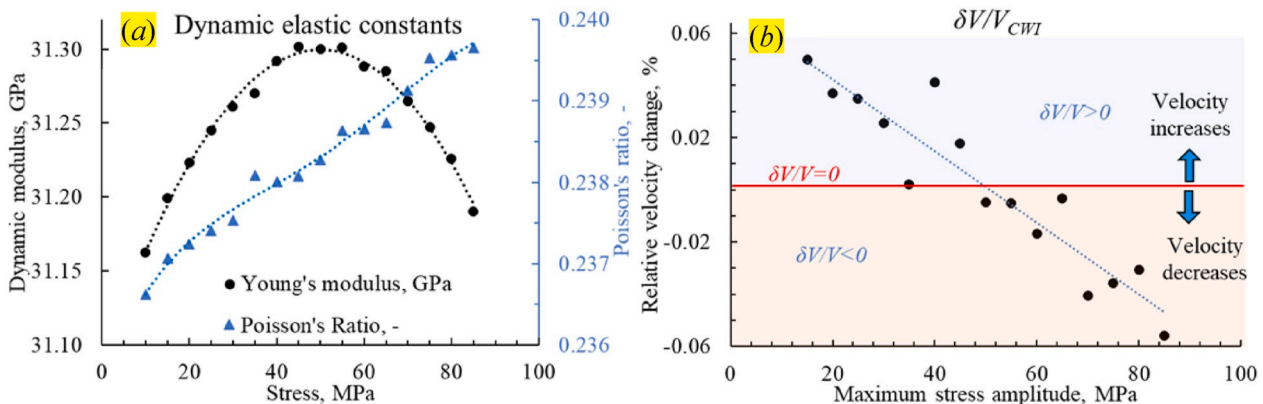


**Fig. 21.** Dynamic constants and the relative changes in the effective velocity of shale specimen UF2 under an increasing-amplitude test.

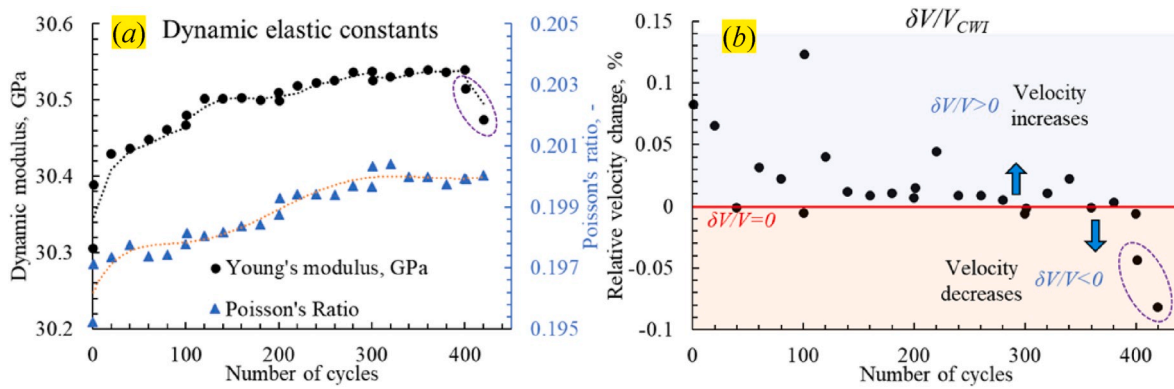


Fig. 22. Dynamic constants and relative changes in the effective velocity of shale specimen UF3 under a constant-amplitude test.

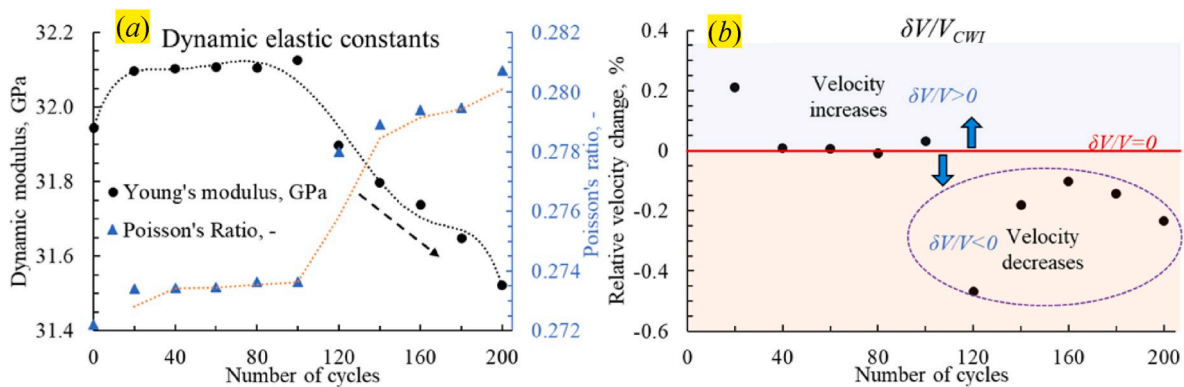


Fig. 23. Dynamic constants and relative changes in the effective velocity of sample Pen09 under a constant-amplitude test.

of the effective velocities, as marked by the purple dashed ellipse in Fig. 22 (b) and Fig. 23 (b). The evolution of the dynamic moduli and the effective velocity are overall consistent with fatigue-induced ultrasonic variation at high-stress cycles for the tested shale specimens as detailed in Section 3.2.2. This is ascribed to the fact that both dynamic Young's modulus and the relative changes in the effective velocity are directly dependent on the perturbations of the P- and S- wave velocities, which are in turn determined by micro-structural perturbations in bulk rocks. In this sense, the two controlling parameters, *i.e.* dynamic elastic constants and relative changes in effective velocity inferred from CWI, can also be used as fatigue indicators to monitor and predict dynamic rock degradation processes.

#### 4. Conclusion

We explored the fatigue behavior and ultrasonic characteristics of three shale specimens monitored in the loading direction, one under an increasing-amplitude of applied load test and the other two under constant-amplitude load tests. The stress-dependent P- and S- wave velocities (monitored in the loading direction) at different stresses were estimated based on first arrivals, while subtle fatigue-induced changes in P- and S- wave velocities at 10 MPa (different unloading paths) were characterized from sensitive CWI coda analysis. Conventional analyses based on stress-strain curves and the evolution of static and dynamic moduli were used to study the fatigue and failure behavior of the three shale specimens. Summary observations are as follows.

The stress-strain response shows hysteretic behavior under cyclic compression. Static elastic moduli are higher during unloading relative to loading (hardening effect). Under loading at constant-amplitude, the hardening effect becomes more apparent with an increase in the maximum stress. However, the evolution of the elastic moduli could not serve as useful and robust indicator of damage to predict fatigue-induced

damage and failure behavior. Poisson's ratio based on stress-strain relation may be a good indicator of fatigue-induced damage under constant-amplitude test; nevertheless, the stress-strain relation is hard to be non-destructively obtained, which is not applicable to detecting failure precursors in the field either.

The P-wave velocity of shale sample UF2 (under increasing-amplitude) at the maximum stress increases with stress *via* the closure of micro-fractures. However, the S-wave velocity, shows a slightly descending trend at high stresses. For sample UF3 under constant-amplitude loading, despite the continuous increase in ultrasonic velocity monitored at high stress amplitudes, the accumulation of fatigue-induced damage due to an increasing number of cycles triggers rock failure at a cyclic maximum stress smaller than the static rock strength. In this sense, the comparison of ultrasonic velocity monitored at different maximum stresses is not a reliable indicator to predict rock failure under cyclic loading.

Variations in ultrasonic velocities monitored at the minimum stress (10 MPa) show an increasing trend at low-stresses and a descending trend at high-stresses. Prior to failure, S-wave velocity shows an apparent descending trend. This could be a good indicator of fatigue and a suitable failure precursor for natural rocks under dynamic loading. In addition, dynamic modulus and relative changes in effective stress inferred from CWI reflect micro-structural perturbations in bulk rocks and thus is well suited as an indicator of fatigue and to monitor and predict dynamic rock degradation. Last but not least, conventional first arrival methods may cause a misleading interpretation of fatigue-induced internal damage.

#### Declaration of competing interest

The authors declare that they have no known competing financial interests or personal relationships that could have appeared to influence

the work reported in this paper.

## Acknowledgement

This work was financially supported by The National Institute of Occupational Safety and Health (NIOSH) under contract No. NIOSH-200-2016-90385. The data used in this paper can be downloaded from the Zenodo website (<http://doi.org/10.5281/zenodo.3572835>).

## Appendix A. Supplementary data

Supplementary data to this article can be found online at <https://doi.org/10.1016/j.ijrmms.2020.104366>.

## References

- Burdine NT. Rock failure under dynamic loading conditions. *Old SPE J.* 1963;3(1): 1–8.
- Zang A, Yoon JS, Stephansson O, Heidbach O. Fatigue hydraulic fracturing by cyclic reservoir treatment enhances permeability and reduces induced seismicity. *Geophys J Int.* 2013;195(2):1282–1287.
- Cerfontaine B, Collin F. Cyclic and fatigue behaviour of rock materials: review, interpretation and research perspectives. *Rock Mech Rock Eng.* 2018;51(2):391–414.
- Bagde MN, Petroš V. Waveform effect on fatigue properties of intact sandstone in uniaxial cyclical loading. *Rock Mech Rock Eng.* 2005;38(3):169–196.
- Tien YM, Lee D-H, Juang CH. Strain, pore pressure and fatigue characteristics of sandstone under various load conditions. In: *International Journal of Rock Mechanics and Mining Sciences & Geomechanics Abstracts*. vol. 27. Elsevier; 1990:283–289.
- Momeni A, Karakus M, Khanlari GR, Heidari M. Effects of cyclic loading on the mechanical properties of a granite. *Int J Rock Mech Min Sci.* 2015;100(77):89–96.
- Xiao J-Q, Ding D-X, Jiang F-L, Xu G. Fatigue damage variable and evolution of rock subjected to cyclic loading. *Int J Rock Mech Min Sci.* 2010;3(47):461–468.
- Zoback MD, Byerlee JD. The effect of cyclic differential stress on dilatancy in Westerly granite under uniaxial and triaxial conditions. *J Geophys Res.* 1975;80(11): 1526–1530.
- Liu E, He S. Effects of cyclic dynamic loading on the mechanical properties of intact rock samples under confining pressure conditions. *Eng Geol.* 2012;125:81–91.
- Gatelier N, Pellet F, Loret B. Mechanical damage of an anisotropic porous rock in cyclic triaxial tests. *Int J Rock Mech Min Sci.* 2002;39(3):335–354.
- Le J-L, Manning J, Labuz JF. Scaling of fatigue crack growth in rock. *Int J Rock Mech Min Sci.* 2014;72:71–79.
- Bernabé Y, Revil A. Pore-scale heterogeneity, energy dissipation and the transport properties of rocks. *Geophys Res Lett.* 1995;22(12):1529–1532.
- Eberhardt E, Stead D, Stimpson B. Quantifying progressive pre-peak brittle fracture damage in rock during uniaxial compression. *Int J Rock Mech Min Sci.* 1999;36(3): 361–380.
- Heap MJ, Faulkner DR. Quantifying the evolution of static elastic properties as crystalline rock approaches failure. *Int J Rock Mech Min Sci.* 2008;45(4):564–573.
- Jiang X, Shu-chun L, Yun-qi T, Xiao-jun T, Xin W. Acoustic emission characteristic during rock fatigue damage and failure. *Procedia Earth Planet Sci.* 2009;1(1): 556–559.
- Mitchell TM, Faulkner DR. Experimental measurements of permeability evolution during triaxial compression of initially intact crystalline rocks and implications for fluid flow in fault zones. *J Geophys Res Solid Earth.* 2008;113(B11).
- Rao M, Ramana YV. A study of progressive failure of rock under cyclic loading by ultrasonic and AE monitoring techniques. *Rock Mech Rock Eng.* 1992;25(4):237–251.
- Chen Y, Zuo J, Guo B, Guo W. Effect of cyclic loading on mechanical and ultrasonic properties of granite from Maluanshan Tunnel. *Bull Eng Geol Environ.* 2019;1–13.
- Jia H, Wang E, Song D, Wang X, Ali M. Precursory changes in wave velocity for coal and rock samples under cyclic loading. *Results Phys.* 2019;12:432–434.
- Grêt A, Snieder R, Scales J. Time-lapse monitoring of rock properties with coda wave interferometry. *J Geophys Res Solid Earth.* 2006;111(B3).
- Snieder R. Coda wave interferometry and the equilibration of energy in elastic media. *Phys Rev E.* 2002;66(4):46615.
- Aki K, Chouet B. Origin of coda waves: source, attenuation, and scattering effects. *J Geophys Res.* 1975;80(23):3322–3342.
- Snieder R, Grêt A, Douma H, Scales J. Coda wave interferometry for estimating nonlinear behavior in seismic velocity. *Science.* 2002;295(5563):2253–2255.
- Roberts PM, Phillips WS, Fehler MC. Development of the active doublet method for measuring small velocity and attenuation changes in solids. *J Acoust Soc Am.* 1992;91(6):3291–3302.
- Snieder R. The theory of coda wave interferometry. *Pure Appl Geophys.* 2006;163(2-3):455–473.
- Griffiths L, Lengliné O, Heap MJ, Baud P, Schmittbuhl J. Thermal cracking in Westerly Granite monitored using direct wave velocity, coda wave interferometry, and acoustic emissions. *J Geophys Res Solid Earth.* 2018;123(3):2246–2261.
- Aki K. Theory of earthquake prediction with special reference to monitoring of the quality factor of lithosphere by the coda method. *Practical Approaches to Earthquake Prediction and Warning.* Springer; 1985:219–230.
- Jin A, Aki K. Temporal change in coda Q before the Tangshan earthquake of 1976 and the Haicheng earthquake of 1975. *J Geophys Res Solid Earth.* 1986;91(B1): 665–673.
- Grêt A, Snieder R, Aster RC, Kyle PR. Monitoring rapid temporal change in a volcano with coda wave interferometry. *Geophys Res Lett.* 2005;32(6).
- Snieder R, Hagerty M. Monitoring change in volcanic interiors using coda wave interferometry: application to Arenal Volcano, Costa Rica. *Geophys Res Lett.* 2004;31(9).
- Zhu T, Ajo-Franklin J, Daley TM, Marone C. Dynamics of geologic CO<sub>2</sub> storage and plume motion revealed by seismic coda waves. *Proc Natl Acad Sci Unit States Am.* 2019;116(7):2464–2469.
- Wang B, Zhu P, Chen Y, Niu F, Wang B. Continuous subsurface velocity measurement with coda wave interferometry. *J Geophys Res Solid Earth.* 2008;113(B12).
- Olsen-Kettle L. Quantifying the orthotropic damage tensor for composites undergoing damage-induced anisotropy using ultrasonic investigations. *Compos Struct.* 2018;204:701–711.
- Olsen-Kettle L. Using ultrasonic investigations to develop anisotropic damage models for initially transverse isotropic materials undergoing damage to remain transverse isotropic. *Int J Solid Struct.* 2018;138:155–165.
- Olsen-Kettle L. Bridging the macro to mesoscale: evaluating the fourth-order anisotropic damage tensor parameters from ultrasonic measurements of an isotropic solid under triaxial stress loading. *Int J Damage Mech.* 2019;28(2):219–232.
- Sarout J, Cazes E, Delle Piane C, Arena A, Esteban L. Stress-dependent permeability and wave dispersion in tight cracked rocks: experimental validation of simple effective medium models. *J Geophys Res Solid Earth.* 2017;122(8):6180–6201.
- Adam L, van Wijk K, Otheim T, Batzle M. Changes in elastic wave velocity and rock microstructure due to basalt-CO<sub>2</sub>-water reactions. *J Geophys Res Solid Earth.* 2013; 118(8):4039–4047.
- Singh J, Curtis A, Zhao Y, Cartwright-Taylor A, Main I. Coda wave interferometry for accurate simultaneous monitoring of velocity and acoustic source locations in experimental rock physics. *J Geophys Res Solid Earth.* 2019;124(6):5629–5655.
- Sens-Schönfelder C, Wegler U. Passive image interferometry and seasonal variations of seismic velocities at Merapi Volcano, Indonesia. *Geophys Res Lett.* 2006;33(21).
- Larose E, Hall S. Monitoring stress related velocity variation in concrete with a 2×10–5 relative resolution using diffuse ultrasound. *J Acoust Soc Am.* 2009;125(4): 1853–1856.
- Hadziioannou C, Larose E, Coutant O, Roux P, Campillo M. Stability of monitoring weak changes in multiply scattering media with ambient noise correlation: laboratory experiments. *J Acoust Soc Am.* 2009;125(6):3688–3695.
- Kendrick JE, Smith R, Sammonds P, Meredith PG, Dainty M, Pallister JS. The influence of thermal and cyclic stressing on the strength of rocks from Mount St. Helens, Washington. *Bull Volcanol.* 2013;75(7):728.
- Yang S-Q, Ranjith PG, Huang Y-H, et al. Experimental investigation on mechanical damage characteristics of sandstone under triaxial cyclic loading. *Geophys J Int.* 2015;201(2):662–682.
- Royer-Carfagni G, Salvatore W. The characterization of marble by cyclic compression loading: experimental results. *Mech Cohesive-frictional Mater An Int J Exp Model Comput Mater Struct.* 2000;5(7):535–563.
- Heap MJ, Faulkner DR, Meredith PG, Vinciguerra S. Elastic moduli evolution and accompanying stress changes with increasing crack damage: implications for stress changes around fault zones and volcanoes during deformation. *Geophys J Int.* 2010; 183(1):225–236.
- Trippetta F, Collettini C, Meredith PG, Vinciguerra S. Evolution of the elastic moduli of seismogenic Triassic Evaporites subjected to cyclic stressing. *Tectonophysics.* 2013; 592:67–79.
- Walsh JB. The effect of cracks on the uniaxial elastic compression of rocks. *J Geophys Res.* 1965;70(2):399–411.
- Niederleithinger E, Wang X, Herbrand M, Müller M. Processing ultrasonic data by coda wave interferometry to monitor load tests of concrete beams. *Sensors.* 2018;18(6):1971.
- Bassil A, Wang X, Chapeleau X, Niederleithinger E, Abraham O, Leduc D. Distributed fiber optics sensing and coda wave interferometry techniques for damage monitoring in concrete structures. *Sensors.* 2019;19(2):356.
- Priou R, Bakulin A, Bakulin V. Nonlinear rock physics model for estimation of 3D subsurface stress in anisotropic formations: theory and laboratory verification. *Geophysics.* 2004;69(2):415–425.
- Fjær E. Static and dynamic moduli of a weak sandstone. *Geophysics.* 2009;74(2): WA103–WA112.
- Wang Y, Li CH. Investigation of the P-and S-wave velocity anisotropy of a Longmaxi formation shale by real-time ultrasonic and mechanical experiments under uniaxial deformation. *J Petrol Sci Eng.* 2017;158:253–267.
- Planès T, Larose E. A review of ultrasonic Coda Wave Interferometry in concrete. *Cement Concr Res.* 2013;53:248–255.
- Antonaci P, Bocca P, Masera D. Fatigue crack propagation monitoring by Acoustic Emission signal analysis. *Eng Fract Mech.* 2012;81:26–32.
- Heap MJ, Vinciguerra S, Meredith PG. The evolution of elastic moduli with increasing crack damage during cyclic stressing of a basalt from Mt. Etna volcano. *Tectonophysics.* 2009;471(1-2):153–160.